Available online at www.sciencedirect.com
SCIENCE DIRECT
Icarus 172 (2004) 625–640
ICARUS
www.elsevier.com/locate/icarus

On the resurfacing of Ganymede by liquid–water volcanism

Adam P. Showman [a,*], Ignacio Mosqueira [b], James W. Head III [c]

[a] *Department of Planetary Sciences, Lunar and Planetary Laboratory, University of Arizona, Tucson, AZ 85721, USA*
[b] *NASA Ames Research Center 245-3, Moffett Field, CA 94035, USA*
[c] *Department of Geological Sciences, Brown University, Providence, RI 02912, USA*

Received 6 December 2003; revised 19 July 2004

Available online 15 September 2004

Abstract

A long-popular model for producing Ganymede's bright terrain involves flooding of low-lying graben with liquid water, slush, or warm, soft ice. The model suffers from major problems, however, including the absence of obvious near-surface heat sources, the negative buoyancy of liquid water, and the lack of a mechanism for confining the flows to graben floors. We present new models for cryovolcanic resurfacing to overcome these difficulties. Tidal heating within an ancient Laplace-like orbital resonance (Showman and Malhotra 1997, Icarus 127, 93; Showman et al., 1997, Icarus 129, 367) provides a plausible heat source and could allow partial melting to occur as shallow as 5–10 km depth. Our favored mechanism for delivering this water to the surface invokes the fact that topography—such as a global set of graben—causes subsurface pressure gradients that can pump water or slush upward onto the floors of topographic lows (graben) despite the negative buoyancy of the liquid. These eruptions can occur only within the topographic lows; furthermore, as the low areas become full, the pressure gradients disappear and the resurfacing ceases. This provides an explanation for the observed straight dark-bright terrain boundaries: water cannot overflow the graben, so resurfacing rarely embays craters or other rough topography. Pure liquid water can be pumped to the surface from only 5–10 km depth, but macroscopic bodies of slush ascending within fractures can reach the surface from much greater depths due to the smaller negative buoyancy of slush. A challenge for these models is the short predicted gravitational relaxation timescale of topographic features at high heat flows; the resurfacing must occur before the graben topography disappears. We also evaluate alternate resurfacing mechanisms, such as pumping of liquid water to the surface by thermal expansion stresses and buoyant rise of water through a silicate-contaminated crust that is denser than liquid water, and conclude that they are unlikely to explain Ganymede's bright terrain.

Keywords: Satellites of Jupiter; Ganymede; Volcanism; Tides, solid body; Surfaces, satellite

1. Introduction

Voyager and Galileo images have shown that Ganymede, the Solar System's largest satellite, experienced a violent geological history. About 35% of Ganymede is covered with ancient, heavily cratered dark terrain that superficially resembles the geologically dead surface of Callisto. The remaining 65%, however, consists of bright terrain with relatively low crater densities that indicates the occurrence of a major geological upheaval (Pappalardo et al., 2004; Showman and Malhotra, 1999; McKinnon and Parmentier, 1986; Collins et al., 2000), perhaps as recently as 1 Ga ago (Zahnle et al., 1998). In most places this bright terrain is heavily grooved and tectonized (Fig. 1). Individual resurfaced units within bright terrain are typically ∼ 100 km wide, whereas the grooves within these units are ∼ 1–10 km wide (Shoemaker et al., 1982; Patel et al., 1999). The mechanisms that replaced the ancient dark terrain with bright terrain and deformed it with grooves are poorly understood and represent one of the most important unsolved problems in icy satellite geology.

The prevailing Voyager-era view was that bright terrain formed by flooding of a global set of graben—i.e., low-lying, fault-bounded blocks produced by lithospheric extension—with liquid water, slush, or warm, soft ice (Golombek and

* Corresponding author. Fax: (520)-621-4933.
E-mail address: showman@lpl.arizona.edu (A.P. Showman).

0019-1035/$ – see front matter
doi:10.1016/j.icarus.2004.07.011

Allison, 1981; Parmentier et al., 1982; Murchie et al., 1986). This model naturally explains the high albedo and low crater densities of bright terrain. Because the cryovolcanic flows would terminate against the fault scarps, it also explains the fact that bright–dark terrain boundaries are sharp and do not embay preexisting topography within the dark terrain (Fig. 1). Such cryovolcanism also provides the best explanation for observations that some lightly tectonized resurfaced lanes of width ∼ 30–100 km are flat, horizontal, and lie 1–2 km lower than the surrounding terrain (Schenk et al., 2001; Shoemaker et al., 1982) and that young bright-terrain lanes sometimes embay ridges and troughs on adjacent older bright terrains (Schenk et al., 2001).

High-resolution Galileo images have reopened the debate about bright-terrain formation mechanisms. Although a few isolated cryovolcanic flow features have been discovered (Schenk and Moore, 1995; Head et al., 1998; Schenk et al., 2001), there is little evidence for ubiquitous volcanic landforms on Ganymede. Furthermore, several regions where intense tectonism caused destruction of underlying craters or bright terrain have been found (Pappalardo and Collins, 1999; Pappalardo et al., 1998). The tectonically resurfaced areas generally exhibit numerous triangular ridges and troughs of ∼ 1-km wavelength, which probably resulted from tilt-block normal faulting that caused the destruction of the pre-existing landforms (Pappalardo et al., 1998; Pappalardo and Collins, 1999). These observations have led to the suggestion that tectonic resurfacing may have been widespread, hence mitigating or removing the necessity of cryovolcanism (Head et al., 1997, 2002; Prockter, 2001; Pappalardo et al., 2004). But many resurfaced terrains are relatively smooth, suggesting that they have been only lightly tectonized (Figs. 1, 2), and tectonic resurfacing has difficulty explaining these regions unless cryovolcanism occurred concurrently with the tectonism (e.g., Harpagia Sulcus; see Head et al., 2002). Therefore, a mechanism for cryovolcanism is still needed.

However, there are major difficulties in understanding how widespread cryovolcanic resurfacing can occur. Liquid water is denser than ice, so any liquid produced at even shallow depths will percolate downward, away from the surface, and be unavailable for volcanic resurfacing. This contrasts with the situation on terrestrial planets, where silicate melt is less dense than the solid and volcanism can occur relatively easily. Furthermore, the primary melt-production mechanism on Earth—pressure-release melting associated with adiabatic ascent of mantle material toward the surface—is impossible on icy satellites. The decrease in ice-melting temperature with increasing pressure instead causes *freezing* of partially molten ice advected toward the surface. Although this freezing is incomplete for large melt fractions (∼ 1% freezing occurs for every 10 km of adiabatic ascent), it ensures that melt can never be produced by adiabatic ascent alone, as occurs on terrestrial planets. A strong source of internal heating is instead required to produce liquid water near the surface.

These problems persist even when alternate compositions are considered. Ganymede's ice may contain salts, but for

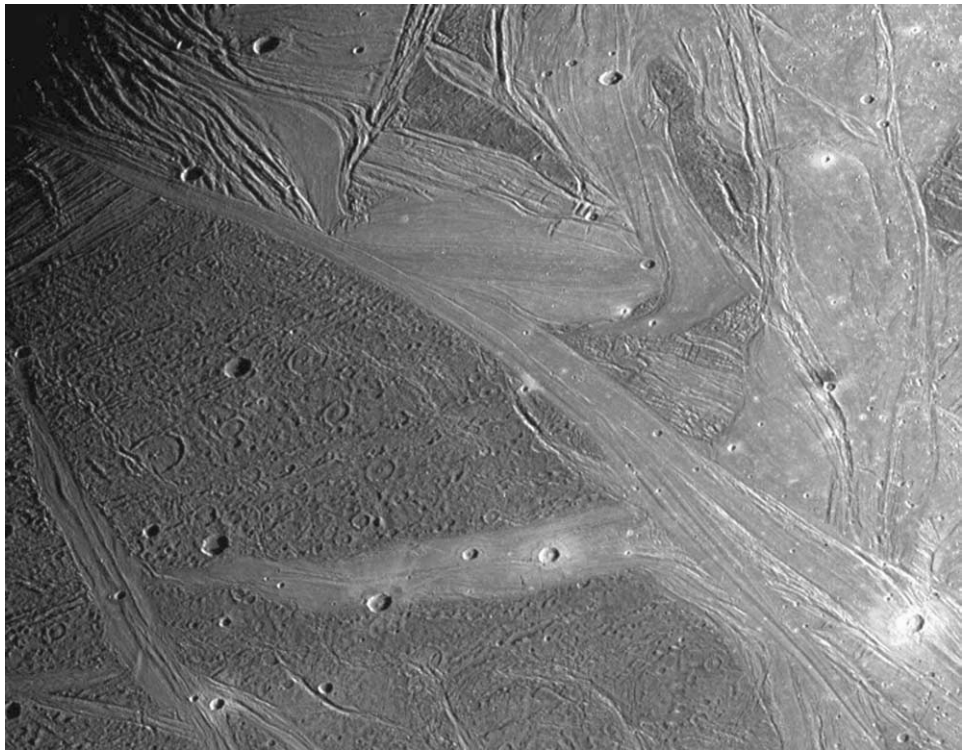

Fig. 1. Regional Galileo view of Ganymede bright and dark terrain. Many patches of the bright terrain are smooth, suggesting volcanism. The image, which is centered at 43° latitude and 194° longitude, covers an area approximately 664 by 518 km at 940 m pixel^{-1}.

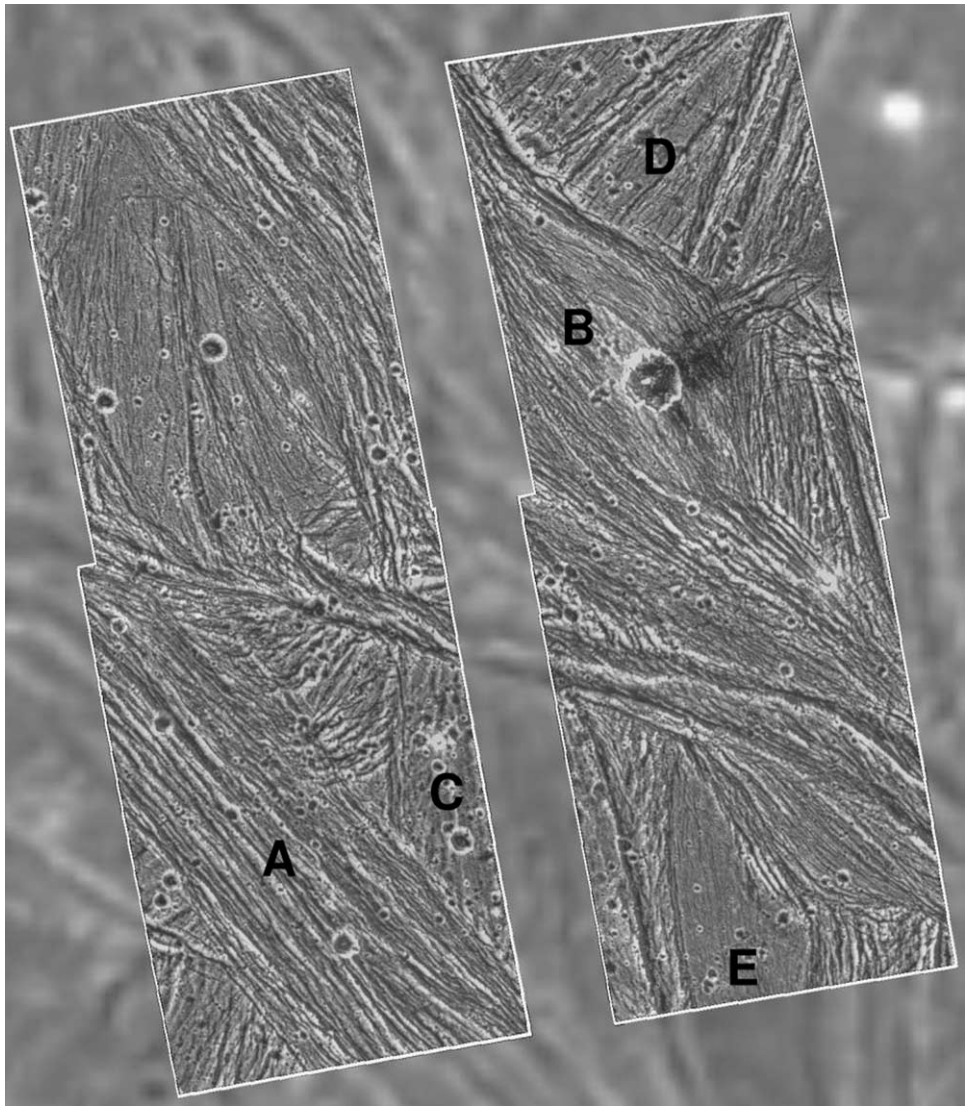

Fig. 2. High-resolution Galileo image of grooved terrain in Uruk Sulcus (11° N, 170° W) spanning 120 by 110 km at 74 m pixel^{-1}. Some regions (A, B) contain numerous ridges and troughs of triangular cross section, which are apparently associated with strains up to 50%. The tectonic formation of these terrains apparently destroyed portions other terrains (C, D), hence tectonically resurfacing them (Pappalardo et al., 1998). In contrast, (D) exhibits horst-and-graben faulting and (E) exhibits faint fracturing with no obvious macroscopic strain. Removal of pre-existing craters and other landforms in (D) and (E) probably required volcanic resurfacing acting in concert with the tectonism.

plausible compositions, salty liquid water is still denser than salty ice of the same composition (Kargel, 1991). And although a eutectic ammonia–water melt is almost neutrally buoyant relative to ice (Croft et al., 1988), Ganymede is unlikely to have formed with sufficient ammonia to allow massive ammonia–water flooding of the surface. Addition of salts or ammonia can lower the freezing temperature, but the phenomenon of pressure-release freezing remains (Hogenboom et al., 1995, 1997).

A mechanism for producing and transporting massive amounts of liquid water, slush, or soft ice onto the surface is a necessary, but not sufficient, condition for explaining Ganymede's bright terrain by cryovolcanic processes. In addition, the mechanism must explain how the volcanic floods were confined so completely to graben floors—as required to explain the generally straight dark–bright terrain boundaries that are nearly universal on Ganymede. Two specific conditions must be met:

(1) Although the eruptions must be effusive enough to submerge craters on the graben floors, they must not overflow the graben—otherwise, chaotic bright–dark terrain boundaries that embay topography would be produced. Extremely few such features are observed on Ganymede, however (Allison and Clifford, 1987). This suggests the existence of a shut-off mechanism that terminated the eruptions before the graben overflowed.
(2) Not only must graben be flooded, but the *eruption locations* must be predominantly confined to the graben floors. Any mechanism that allows eruption of cryvolcanic materials within topographic highs is inconsistent with observations, because the erupted materials would

flow downhill toward topographic lows, leaving rilles or other obvious flow markings (which are common on the terrestrial planets but absent on Ganymede's dark terrain). What is needed is a mechanism that allows volcanic eruptions in topographic lows but discourages them within topographic highs.

A buoyant melt could presumably rise to the surface anywhere, so one might argue that the observations are best explained with a melt that is denser than the solid (Allison, 1982). This argument is incomplete, however, because no plausible mechanism for transporting large quantities of dense melt onto Ganymede's surface has been proposed, nor is it clear why the eruptions would be confined to graben floors.

Although Ganymede currently experiences negligible tidal heating (due to its low orbital eccentricity of 0.0015), Ganymede's eccentricity may have been high enough in the past for tidal heating and flexing to drive internal activity. This heating might aid formation of bright terrain and explain why Ganymede's surface differs so drastically from Callisto's. Showman and Malhotra (1997) and Malhotra (1991) describe the most plausible scenario, in which Io, Europa, and Ganymede pass through a Laplace-like resonance before evolving into the presently observed Laplace resonance. These Laplace-like resonances could pump Ganymede's eccentricity to ~ 0.01–0.04 depending on the tidal Q of Ganymede and Jupiter, producing mean heating up to $\sim 10^{12}$ W and tidal flexing stresses up to a bar. Showman et al. (1997) coupled an interior model of Ganymede to the orbital evolution and showed that the ancient tidal heating could cause formation of a massive internal ocean, satellite expansion up to $\sim 1\%$, and consequent lithospheric deformation (e.g., production of graben).

For cryovolcanic resurfacing, the key effect of tidal heating is the likely production of near-surface liquid water, slush, or warm, soft ice. Figure 3 shows the steady-state eccentricities and tidal dissipation rates (expressed as fluxes through Ganymede's surface) for three different resonances from Showman and Malhotra (1997). If Jupiter's tidal dissipation factor, Q_J, is near its time-averaged lower limit of 3×10^4 (Goldreich and Soter, 1966), then tidal-heating fluxes could have reached 80 mW m^{-2}. In a conductive ice shell with a surface temperature of 120 K and a thermal conductivity of $567/T$ W m^{-1}, appropriate to ice, these fluxes would imply partial melting at depths as shallow as 6 km. Even if the time-averaged value of Q_J exceeds 10^5, orbital-geophysical feedbacks may have allowed temporary (10^7 year-long), order-of-magnitude increases in the tidal-heating rate (Showman et al., 1997). Q_J may also vary in time (e.g., Stevenson, 1983; Ioannou and Lindzen, 1993; Houben et al., 2001), and near-surface partial melting could have occurred during intervals when Q_J was low. Furthermore, if the lithosphere comprises rigid plates separated by weak zones, then enhanced tidal heating, and shallow partial melting, would occur at these weak zones (e.g.,

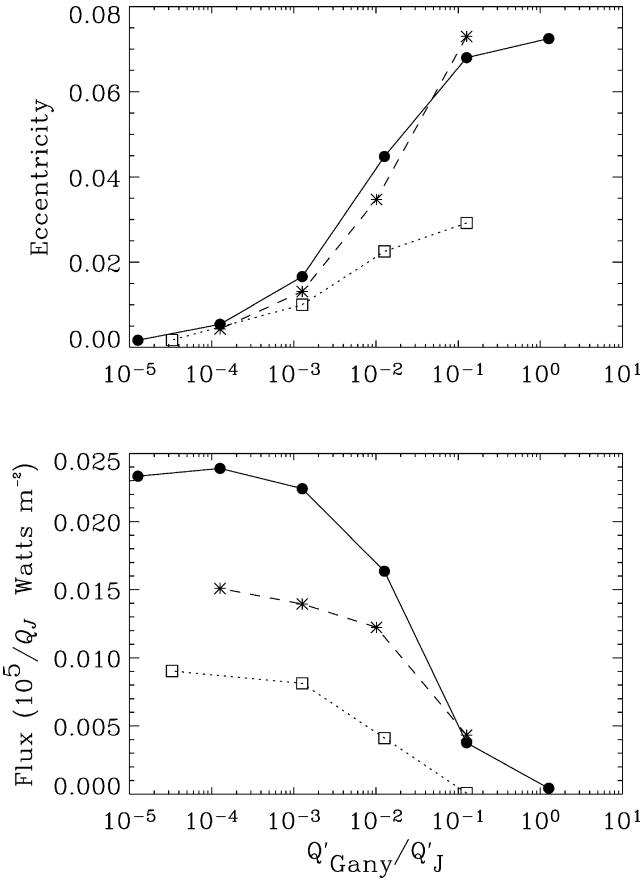

Fig. 3. Steady-state eccentricity and tidal-heating rate, expressed as a power per area through the surface, experienced by Ganymede during passage through a Laplace-like resonance. Horizontal axis is the ratio of Q' for Ganymede to that for Jupiter, where $Q' \equiv Q/k$, Q is the tidal dissipation factor, and k is the second-degree Love number. Solid, dashed, and dotted curves refer to $\omega_1/\omega_2 \approx 2$, 3/2, and 1/2 Laplace-like resonances, respectively, where $\omega_1 \equiv 2n_2 - n_1$, $\omega_2 \equiv 2n_3 - n_2$, and n_1, n_2, and n_3 are the mean motions of Io, Europa, and Ganymede, respectively. After Showman and Malhotra (1997).

Nimmo and Gaidos, 2002). Estimates of the elastic thickness at the edges of grooved terrain, based on flexural models, leads to heat flux estimates at the time of bright-terrain formation of ~ 100 mW m^{-2}, implying thermal gradients of ~ 30 K km^{-1} (Nimmo et al., 2002). Similarly, models for formation of the pervasive 5–10 km-wavelength "Voyager-scale" grooves from a necking instability can only succeed when the lithospheric thermal gradient exceeds ~ 20 K km^{-1} (Collins et al., 1998; Dombard and McKinnon, 2001). The bottom line is that partial melting at depths of 5–10 km is a plausible outcome of an ancient orbital resonance and seems consistent with inferences from surface geology. The question then becomes: how might this material reach the surface?

In this paper, we evaluate possible mechanisms for cryovolcanic resurfacing. Our favored resurfacing mechanism invokes the fact that topography, such as a global set of graben, induces subsurface pressure gradients that can pump negatively-buoyant liquid water or slush upward into the

graben floors. The model naturally confines cryovolcanic eruptions to low-lying regions; furthermore, the pressure gradients that cause resurfacing cease as the graben fill, shutting off the resurfacing before the graben overflow. We also evaluate alternate resurfacing mechanisms, such as pumping of liquid water to the surface by thermal expansion stresses and buoyant rise of water through a silicate-contaminated crust that is denser than liquid water, although these mechanisms are less favorable. We describe the "topographic pumping" resurfacing scenario in Section 2 and the alternate resurfacing mechanisms in Section 3.

2. Topographic pumping of liquid water or slush

2.1. Topographic resurfacing by liquid water

When partial melting occurs, liquid water forms an interconnected network of pores, which allows the liquid to be flushed from the solid matrix. Because the liquid water is negatively buoyant, the liquid would percolate downward in the absence of external effects. However, topography, such as a global set of downdropped graben, causes subsurface stress fields that, under appropriate conditions, can pump negatively buoyant liquid water upward. Here we illustrate how this process can occur.

Melting takes place first along grain boundaries, and we envision that the liquid water produced during tidal heating initially exists within an interconnected network of melt-filled pores, at grain boundaries, that constitute only a small fraction of the total volume. Experiments with ice indicate that when melting occurs the pores form channels of triangular cross section at three-grain intersections. The angle formed by the solid–liquid interfaces at the tips of the triangular channels (the dihedral angle) is about 25°–40° (Ketcham and Hobbs, 1969; Walford et al., 1987; Walford and Nye, 1991; Mader, 1992), which implies that the channels form an interconnected network even for arbitrarily small melt fractions (e.g., Stevenson and Scott, 1991). In salty ice, experiments show that the liquid may exist in isolated pores (analogous to the bubbles in Swiss cheese) at melt fractions less than about 5%; melt-filled pores form an interconnected network only at melt fractions exceeding 5% (Golden et al., 1998). In either case, once an interconnected network forms, the permeability depends strongly on the melt fraction, increasing as the melt fraction to the second or third power (Stevenson and Scott, 1991). Once the melt fraction—hence permeability—is great enough, the melt can be flushed from the matrix in response to melt-matrix buoyancy or external forces. On Earth, such melt percolation, which is upward because the melt is buoyant, supplies the magma that drives volcanism at mid-ocean ridges and elsewhere. Beneath mid-ocean ridges, the balance of melt production and percolation leads to melt fractions of order $\sim 10^{-2}$ within the partially molten zone (Turcotte and Schubert, 2002, pp. 402–405).

The equations governing the coupled flow of a melt and matrix have been derived by several groups over the past twenty years (e.g., McKenzie, 1984; Scott, 1988; Stevenson and Scott, 1991). The momentum equation governing the relative flow of melt and matrix, which is essentially Darcy's law, can be written in general form as

$$f\left(v_i^{\mathrm{liq}} - v_i^{\mathrm{sol}}\right) = -\frac{k}{\eta^{\mathrm{liq}}}\left[\frac{\partial p^{\mathrm{liq}}}{\partial x_i} + g\rho^{\mathrm{liq}}\delta_{iz}\right], \tag{1}$$

where f is the melt fraction (equivalent to porosity), k is the permeability, g is gravity, p^{liq}, η^{liq}, and ρ^{liq} are the pressure, viscosity, and density of the melt, δ_{ij} is the Kronecker delta, v_i^{liq} and v_i^{sol} are the true velocities of the melt and matrix, respectively, x_i are the spatial coordinates, z is height, and $i = 1$, 2, and 3 are the coordinate indices. If the matrix is rigid, then large melt-matrix pressure differences can be sustained. At the opposite extreme, if the matrix has low viscosity, then melt-matrix pressure differences will drive deformation that tends to lessen the pressure differences. A useful limit to think about is one where this process is so effective that the pressure in the liquid is equal to the pressure in the matrix. In this case, the vertical pressure gradient in the melt is simply $-\bar{\rho}g$, where $\bar{\rho} \equiv f\rho^{\mathrm{liq}} + (1-f)\rho^{\mathrm{sol}}$ is the mean density of the matrix-melt mixture and ρ^{sol} is the density of the matrix. When summed with the weight of the melt, this gives a pressure gradient available for driving migration equal to the buoyancy of the melt relative to the mixture, which for small melt fraction is just $-g\Delta\rho$, where $\Delta\rho \equiv \rho^{\mathrm{liq}} - \rho^{\mathrm{sol}}$. In the case of partially molten ice, $\Delta\rho$ is positive, and the liquid would percolate downward.

However, in reality, the pressure in the liquid and solid are not necessarily equal; furthermore, matrix deformation can occur, and this deformation alters the pressure field in the melt. Scott (1988) shows that Eq. (1) can be written

$$f\left(v_i^{\mathrm{liq}} - v_i^{\mathrm{sol}}\right) = \frac{k}{\eta^{\mathrm{liq}}}\left[-(1-f)g\Delta\rho\delta_{iz} - \frac{\partial}{\partial x_j}\left\{(1-f)\left(\sigma_{ij}^{\mathrm{sol}} + p^{\mathrm{liq}}\delta_{ij}\right)\right\}\right], \tag{2}$$

where $\sigma_{ij}^{\mathrm{sol}}$ is the stress field within the solid. The expression in square brackets is the pressure gradient available to drive relative flow between the melt and the matrix. The first term is buoyancy and the second term is caused by matrix deformation and melt-fraction gradients (Scott, 1988; Stevenson, 1989).

The stress and velocity fields in the matrix are related by the constitutive law, which we take to be that of a viscous solid (e.g., Scott, 1988):

$$(1-f)\left(\sigma_{ij}^{\mathrm{sol}} + p^{\mathrm{liq}}\delta_{ij}\right) = \left(\zeta - \frac{2}{3}\eta\right)\frac{\partial v_k^{\mathrm{sol}}}{\partial x_k}\delta_{ij} + \eta\left\{\frac{\partial v_i^{\mathrm{sol}}}{\partial x_j} + \frac{\partial v_j^{\mathrm{sol}}}{\partial x_i}\right\}, \tag{3}$$

where ζ and η are the bulk and shear viscosities of the matrix. Repeated indices within any term imply summation over the three coordinates. The equations assume that

the solid and liquid are separately incompressible; however, when the melt fraction is nonzero, compressive stresses in the matrix cause compaction of the matrix and expulsion of melt (hence altering the melt fraction). As a result, the flow divergence $\partial v_k^{\rm sol}/\partial x_k \equiv \nabla\cdot\mathbf{v}^{\rm sol}$ is generally nonzero. The bulk viscosity is associated with these changes in volume, and it is nonzero because expelling melt requires irreversible work. In general both ζ and η are functions of melt fraction.

Using the constitutive law, we can write Darcy's law solely in terms of the velocity fields. In vector notation, the equation becomes

$$f\left(\mathbf{v}^{\rm liq}-\mathbf{v}^{\rm sol}\right)=\frac{k}{\eta^{\rm liq}}\Bigg[-(1-f)g\Delta\rho\mathbf{z} - \nabla\left\{\left(\zeta+\frac{1}{3}\eta\right)\nabla\cdot\mathbf{v}^{\rm sol}\right\}-\nabla\left(\eta\nabla\mathbf{v}^{\rm sol}\right)\Bigg], \tag{4}$$

where $\mathbf{v}^{\rm liq}$ and $\mathbf{v}^{\rm sol}$ are the vector velocities of the melt and matrix and $\mathbf{z}$ is the upward unit vector. Three factors affect the migration of melt relative to solid: the melt-matrix buoyancy, the pressure gradient caused by gradients of matrix volume changes due to expansion and compaction, and the pressure gradient caused by volume-conserving shear deformation of the matrix. These correspond to the first, second, and third terms on the right side of Eq. (4). Matrix deformation affects the pressure gradient in the melt through the last two terms, and under appropriate circumstances these gradients may overcome the negative buoyancy and allow liquid water to rise upward through the ice.

Consider the effects of surface topography. Topography causes subsurface stress fields that induce upward motion of the solid ice underneath topographic lows and downward motion underneath topographic highs, which lessens the topography over time (crater relaxation and postglacial rebound being standard examples). The flow is effectively driven by an ahydrostatic pressure-gradient force $-\nabla(\eta\nabla\mathbf{v}^{\rm sol})$ that points downward beneath topographic highs and upward beneath topographic lows. Because these topographically induced pressure gradients will affect melt drainage (Eq. (4)), the pressure-gradient force associated with matrix flow beneath topographic lows *counteracts* the negative buoyancy of the liquid water. If the ahydrostatic pressure gradients are strong enough, liquid water can percolate upward in topographic lows.

We illustrate this process with a simple two-dimensional analytical solution that assumes constant melt-fraction and viscosity. In reality, the behavior is complex and nonlinear; variations in melt fraction are coupled to the flow field, melting and freezing can occur, and the permeability and viscosity depend strongly on the variables being solved for (melt fraction and temperature). A realistic solution of this problem is a major undertaking that requires numerical simulations, which is beyond the scope of the present study. Our current goal is simply to demonstrate the physical mechanism, and an analytical solution suffices for this purpose.

When melt fraction is constant and melting is ignored, the continuity equation for the matrix becomes

$$\nabla\cdot\mathbf{v}^{\rm sol}=0. \tag{5}$$

This equation implies that we can define a streamfunction for the matrix flow, ψ, and Spiegelman and McKenzie (1987) show that the problem of determining ψ reduces to solution of the biharmonic equation, $\nabla^4\psi=0$, under appropriate boundary conditions. In the limit where the melt fraction f goes toward zero, the melt has negligible influence on the matrix force balance and $\mathbf{v}^{\rm sol}$ is governed by pressure-gradient, viscous, and gravity forces in the matrix alone. The velocity $\mathbf{v}^{\rm sol}$ is then just determined by a standard solution for gravitational relaxation of a one-phase, viscous fluid (e.g., Turcotte and Schubert, 2002, Chapter 6). Let the satellite interior and surface correspond to an infinite half-space with a sinusoidal surface topography $h=h_0\cos(mx)$, where m is the wavenumber equal to 2π over the wavelength, x is horizontal distance, and $h_0 m \ll 1$ (the height of the topography is much less than its wavelength). Half-space geometry is approximately valid assuming the topography has a wavelength smaller than the ice-shell thickness, which, for ice shells ~ 100 km thick, implies wavelengths < 100 km. (Thermal models generally imply that, even during periods of tidal heating, Ganymede's ice shell was probably at least 50 km thick (Showman et al., 1997); nevertheless, in future studies it would be worthwhile to relax the half-space assumption and consider the flow in an ice shell of finite thickness.) The sinusoidal topography considered here provides a crude representation of horst and graben formed by lithospheric extension. We apply a no-slip boundary condition (horizontal speed equals zero) at the surface, appropriate because a stiff lithosphere overlies the partially molten region. With this condition, the matrix velocity $\mathbf{v}^{\rm sol}$ is given by (see Turcotte and Schubert, 2002, pp. 238–240)

$$\mathbf{v}^{\rm sol}=-\frac{\rho g h_0}{2\eta}ze^{mz}\sin(mx)\mathbf{x} - \frac{\rho g h_0}{2\eta m}e^{mz}[1-mz]\cos(mx)\mathbf{z}, \tag{6}$$

where $\mathbf{x}$ and $\mathbf{z}$ are the horizontal and upward unit vectors, respectively. The pressure gradients associated with the topographically induced flow are

$$-\nabla p^{\rm sol}=-\eta\nabla^2\mathbf{v}^{\rm sol} =\rho g h_0 m e^{mz}\left[\sin(mx)\mathbf{x}-\cos(mx)\mathbf{z}\right], \tag{7}$$

where z is height; z is zero at the surface and negative within the interior.

Figures 4 and 5 illustrate the pressure gradients for two specific cases. The top panels illustrate the topography—a two-km peak-to-peak-amplitude sinusoid ($h_0=-1$ km) with 30-km wavelength in Fig. 4a and a four-km peak-to-peak-amplitude sinusoid ($h_0=-2$ km) with 60-km wavelength in Fig. 5a. The middle panels, Figs. 4b and 5b, show $-\nabla p$ as predicted by Eq. (7) based on the topography shown

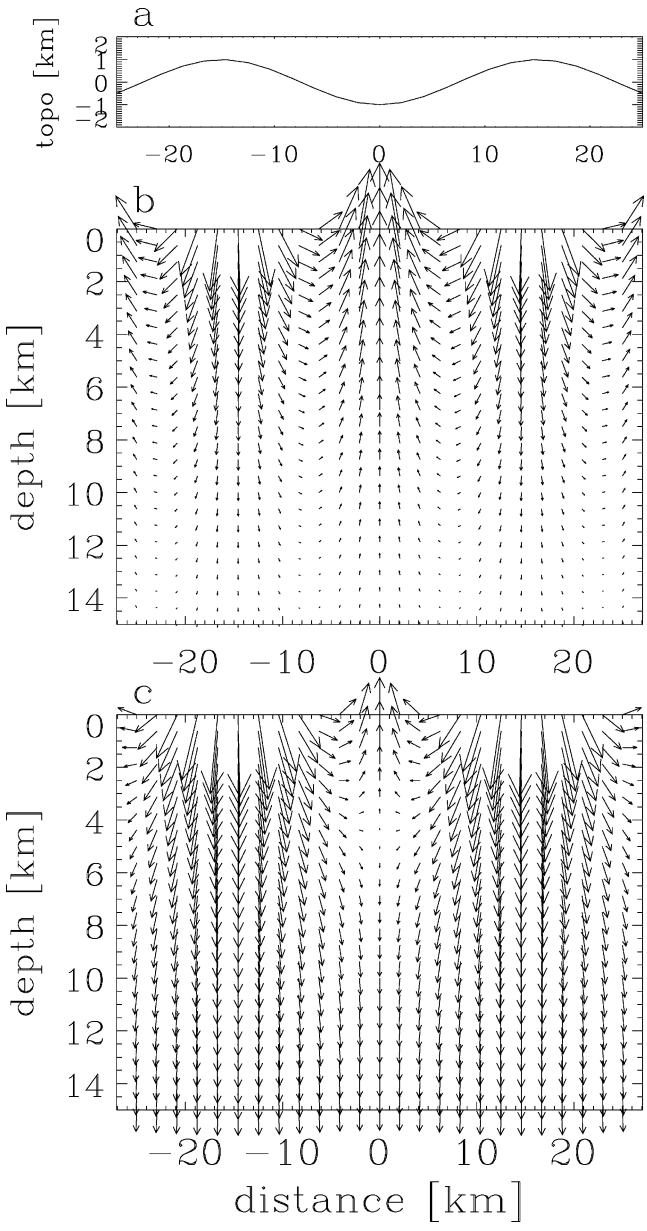

Fig. 4. $-\nabla p$, where p is ahydrostatic pressure, for sinusoidal topography with 30-km wavelength and 2-km peak-to-peak amplitude. (a) The topography. (b) Pressure gradients caused by topography alone. (c) Topographic pressure gradients plus the downward-pointing negative buoyancy ($\Delta\rho g$) of liquid water assuming $\Delta\rho = 80\ \mathrm{kg\,m^{-3}}$. This is the pressure gradient felt by pore–space liquid water. The plot shows that, within topographic lows, liquid water can be pumped to the surface from up to 5 km depth. The largest arrows have amplitudes of 301 and 416 $\mathrm{Pa\,m^{-1}}$ in (b) and (c), respectively, under the assumption that $\rho = 1000\ \mathrm{kg\,m^{-3}}$ and $g = 1.44\ \mathrm{m\,sec^{-2}}$.

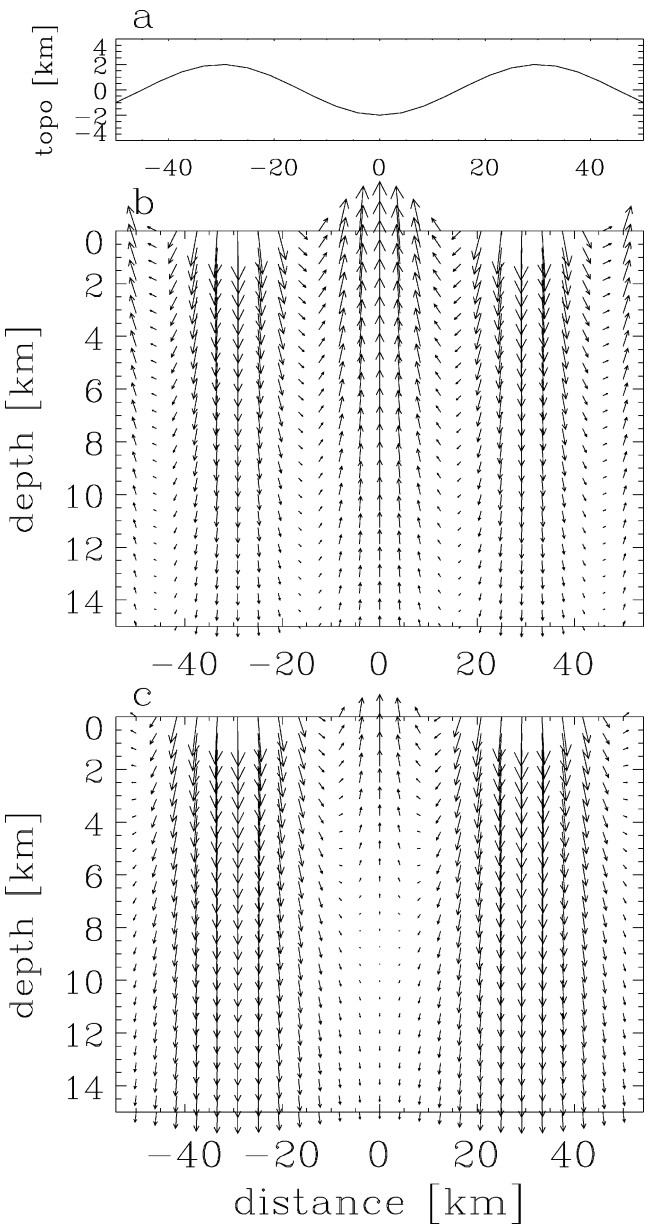

Fig. 5. Same as Fig. 4, but for sinusoidal topography with 60-km wavelength and 4-km peak-to-peak amplitude. Here, liquid water can be pumped into topographic lows from up to 10 km depth. The largest arrows have amplitudes of 301 and 416 $\mathrm{Pa\,m^{-1}}$ in (b) and (c), respectively, under the assumption that $\rho = 1000\ \mathrm{kg\,m^{-3}}$ and $g = 1.44\ \mathrm{m\,sec^{-2}}$.

in the top panels. Because material flows down pressure gradients (i.e., from high to low pressure), $-\nabla p$ gives a measure of the direction in which fluid will flow. As expected for viscous relaxation, the pressure gradients indicate that the ice flows upward underneath topographic lows and downward underneath topographic highs. For a specified wavelength, the pressure gradients are proportional to topographic amplitude. The pressure gradients are greatest near the surface and decay exponentially in depth with a scale height $\mathrm{m^{-1}}$. (This leads to the common understanding that the viscous relaxation of a landform involves motion of material primarily at depths comparable to or less than the landform's width.) For a given topographic amplitude, the surface pressure gradients are greatest for small wavelength and weakest for large wavelength, but the reverse situation is true at great depths because of the wavelength-dependence of the scale height.

Equation (4) implies that the net pressure gradient driving motion in pore–space liquid water is that shown in Figs. 4b and 5b plus the negative buoyancy of the melt, which for

small melt fraction is $-\Delta\rho g\mathbf{z}$. This net pressure gradient (equal to the expression in square brackets from Eq. (4)) is shown in Figs. 4c and 5c assuming that $\Delta\rho = 80\,\mathrm{kg\,m^{-3}}$, relevant for pure liquid water and ice. In the absence of topography, the pore–space liquid water experiences a vertical pressure gradient $-\Delta\rho g$ that causes downward percolation of liquid water. When topography exists, the net pressure gradient still causes downward migration of liquid water at great depths, because the topographic-pressure gradients are weak at large depths. Liquid water will also migrate downward from any depth—even immediately below the surface—underneath topographic highs.

However, underneath topographic lows, the pressure gradients caused by the topography can overwhelm the negative buoyancy of the liquid water, resulting in a net pressure gradient that drives liquid water *upward* into the topographic lows despite the liquid's negative buoyancy. For the topographic amplitudes illustrated in Figs. 4 and 5, the maximum depth from which liquid water can be pumped to the surface is 5–10 km. The fact that melting can occur at 5–10 km depth during plausible tidal heating events suggests that liquid is available to be pumped upward to the surface.

The key advantages of this mechanism for explaining bright terrain are threefold. First, liquid water can be pumped to the surface despite its negative buoyancy. Second, the eruption locations are confined solely to the topographic lows (graben), so the observed paucity of cryovolcanic flow features extending from high-altitude dark terrain into lower-altitude bright terrain is naturally explained. Third, as the graben fill with liquid water (which subsequently freezes into fresh bright terrain), the topography—hence pressure gradients—disappear and the resurfacing automatically ceases. Water therefore cannot overflow the graben. This provides a natural shut-off mechanism that allows the straight boundaries between bright and dark terrain to be explained.

For small, and constant, melt fraction, our simple analytical solution predicts that the maximum depth from which liquid water can reach the surface is

$$d_{\max} = \frac{1}{m}\ln\left(\frac{\Delta\rho}{\rho|h_0|m}\right), \tag{8}$$

which results from equating $\Delta\rho g$ with the vertical pressure gradient at $x = 0$ from Eq. (7). Figure 6 illustrates these maximum depths—as a function of wavelength—for peak-to-peak sinusoidal topographic amplitudes of 4, 2, 1, and 0.5 km (dash–dot, solid, dotted, and dashed lines, respectively). It is clear from Eq. (8) that the maximum depth from which liquid water can be pumped to the surface is independent of viscosity and gravity. For constant topographic amplitude, the maximum depth of pumping increases with wavelength at small wavelengths and decreases with wavelength at large wavelengths, maximizing at an intermediate wavelength of 50–100 km. The reason is as follows. For a given topographic amplitude, small (e.g., < 10 km) wavelengths do not favor pumping: although the amplitudes of the surface pressure gradients are large, the pressure gradients decay rapidly with depth, so liquid can only be pumped if it exists very close to the surface ($<$ 1–2 km depth). Large (> 100 km) wavelengths also do not favor pumping: the pressure gradients extend to great depth, but they are weak because the topographic slopes are small. At intermediate wavelengths, the pressure gradients are great enough to overcome the negative buoyancy of liquid water, and they also extend to reasonable depths. The top panel assumes $\Delta\rho = 80\,\mathrm{kg\,m^{-3}}$ as appropriate for pure ice and water. Some salt systems of eutectic composition have reduced liquid–solid density differences, however; for example, the ternary $MgSO_4$–Na_2SO_4–H_2O eutectic liquid, which contains $\sim 17\%$ $MgSO_4$ and $\sim 4\%$ Na_2SO_4 by weight, has a density only 60 $\mathrm{kg\,m^{-3}}$ greater than that of the corresponding solid, and a similar density contrast holds for the binary eutectic $MgSO_4$–H_2O (Kargel, 1991). Furthermore, it is possible that silicate contamination helps decrease the average liquid–solid density difference (although this configuration may be gravitationally unstable if underlain by cleaner ice). The bottom panel shows the maximum depth of pumping assuming that $\Delta\rho = 40\,\mathrm{kg\,m^{-3}}$. In this case, liquid water can be pumped upward from 10–20 km depth.

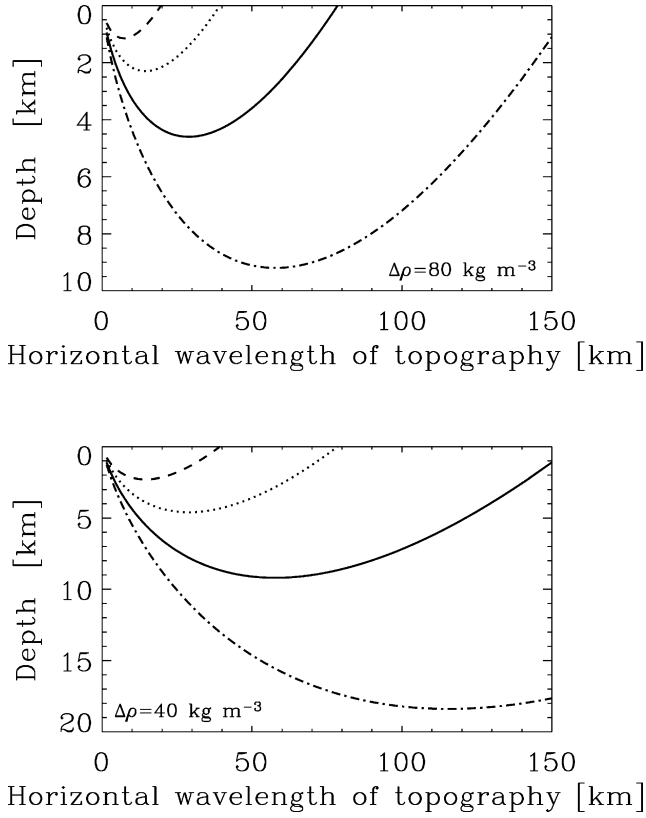

Fig. 6. Maximum depth from which liquid water can be pumped upward versus wavelength of the topography, assumed sinusoidal. Dashed-dot, solid, dotted, and dashed curves correspond to peak-to-peak topographic amplitudes of 4, 2, 1, and 0.5 km, respectively. Top: $\Delta\rho = 0.08\,\mathrm{gm\,cm^{-3}}$. Bottom: $\Delta\rho = 0.04\,\mathrm{gm\,cm^{-3}}$.

The fact that the horizontal wavelength that favors pumping is 50–100 km (Fig. 6) is consistent with the sizes of Ganymede's resurfaced domains, which are typically 30–$\sim$ 100 km wide (Shoemaker et al., 1982). However, it is unlikely that the topography associated with the grooves themselves can allow resurfacing. Individual $\sim$ 5–10 km-wide grooves within bright terrain have peak-to-peak topography typically ranging from 300–700 m (Squyres, 1981). This topography is insufficient to pump water to the surface unless melting occurs within the uppermost $\sim$ 1 km, which is unlikely.

Realistic topography for a flat-floored graben can be expressed as a Fourier superposition of many sinusoids of differing wavelengths, and, because our analytic solution is linear, the corresponding pressure gradients can be calculated from Eq. (7). Figure 7 shows an example for a 20-km-wide graben 2 km deep. Near the surface, the pressure gradients have greatest magnitude at the edges of the graben, but at depth the greatest pressure gradients are at the graben center (Fig. 7b). Interestingly, for $\Delta\rho = 80\ \mathrm{kg\,m^{-3}}$, liquid can be pumped from up to 8 km depth (Fig. 7c), approximately 50% deeper than the maximum depth from which liquid water can reach the surface for sinusoidal topography of the same amplitude (i.e., 2-km peak-to-peak). Similarly, for a 4-km-deep graben that is 50 km across, liquid can ascend from up to 15 km depth, again about 50% greater than the maximum pumping depths for the corresponding sinusoidal case. This enhancement apparently results from the fact that the Fourier integral representing a graben contains long-wavelength sinusoidal components whose peak-to-peak amplitudes (when summed) exceed the graben depth; constructive and destructive interference with the short-wavelengths components then yields the final graben shape (Fig. 7a). Because the pressure gradients associated with the short-wavelength components decay rapidly with depth (Eq. (7)), the main factor determining the maximum depth of pumping is the long-wavelength components. Therefore the large amplitude of these components causes an enhancement in the maximum depth from which liquid can ascend.

What are plausible depths for the graben within which the bright terrain formed? Using stereo images, Schenk et al. (2001) identified smooth resurfaced areas that are 1–2 km lower than the surroundings. Viscous relaxation has probably lessened this topography over time, so the topography immediately after resurfacing would have been even greater. To submerge pre-existing craters, the resurfaced areas must have been flooded to depths of $\sim$ 1 km, implying an original graben depth up to 2–4 km. The mechanism must be able to supply liquid to the surface until the final stages of infill as the resurfacing ceases. 4- and 2-km topography, which are plausible upper limits for the pre- and post-resurfacing graben depths, allow water to reach the surface from 10–20 and 5–10 km depth, respectively, depending on the liquid–solid density contrast.

Consider, to order-of-magnitude, the basic constraints on melt-production rate, permeability, and subsurface melt fraction imposed by the requirement to form bright terrain. Suppose the volumetric tidal heating rate that causes melting is q and that liquid water pumped to the surface originates from a range of depths d. If all of the liquid water produced over this range of depths reaches the surface, then the graben will fill in a time

$$\tau_{\mathrm{fill}} \sim \frac{h\rho L}{qd}, \tag{9}$$

where h is the depth to which the graben are flooded, $L = 3 \times 10^5\ \mathrm{J\,kg^{-1}}$ is the latent heat of melting and ρ is ice den-

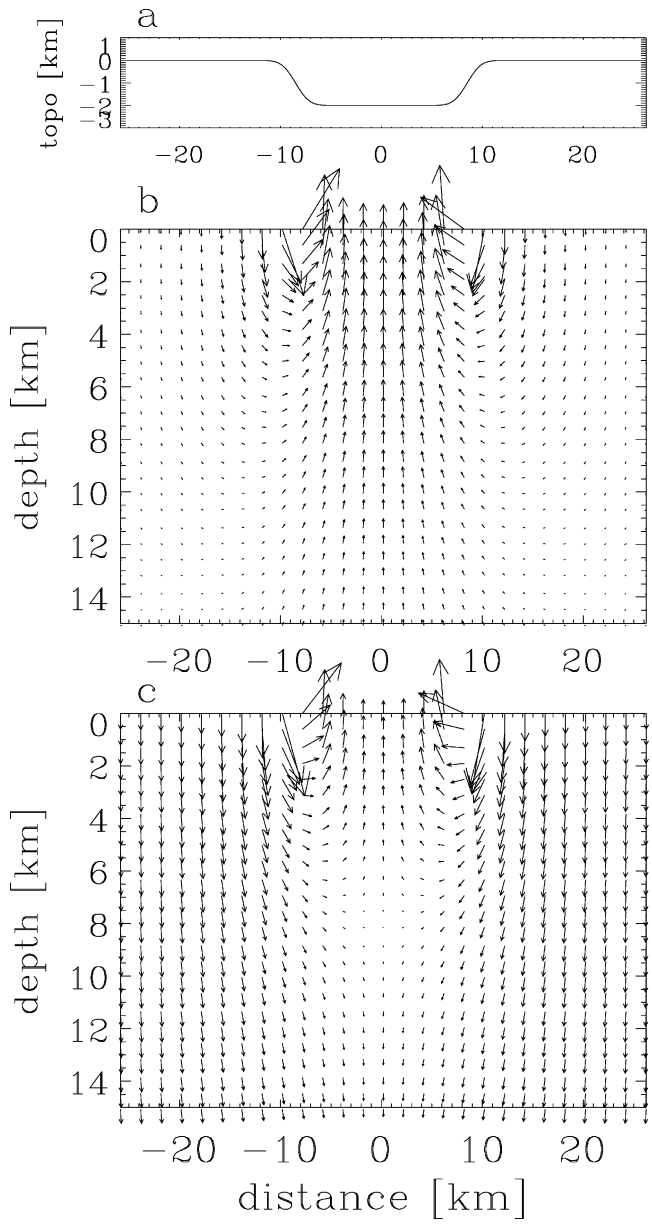

Fig. 7. Same as Fig. 4, but for a 20-km-wide graben 2 km deep. The graben is composed of a superposition of Fourier modes; each mode contributes to the total pressure gradient according to Eq. (7). Here, liquid water can be pumped into the graben from up to 8 km depth if $\Delta\rho = 80\ \mathrm{kg\,m^{-3}}$. The largest arrows have amplitudes of 1090 and 1118 $\mathrm{Pa\,m^{-1}}$ in (b) and (c), respectively, under the assumption that $\rho = 1000\ \mathrm{kg\,m^{-3}}$ and $g = 1.44\ \mathrm{m\,sec^{-2}}$.

sity. Using $d \sim 10$ km, $q \sim 10^{-6}\,\mathrm{W\,m^{-3}}$, and $h \sim 1$ km, then $\tau_{\rm fill} \sim 10^6$ years. In other words, for reasonable tidal heating rates, bright terrain units needed at least 10^6 years to form based purely on the requirement to melt, transport to the surface, and then refreeze a ~ 1 km-deep layer of water. In reality, this lower limit may be even larger, because only a fraction of the liquid water that is produced will reach the surface and only a fraction of the total heat production will lead to melting. There is also large uncertainty in q. The above value is appropriate for soft ice if the tidal-flexing strain amplitude is $0.5–1.5 \times 10^{-5}$, relevant to an orbital eccentricity of 0.01–0.02.

If there is a steady-state between the rate of liquid–water production and transport to the surface, then from Eq. (4) the required permeability is

$$k \sim \frac{h\eta^{\rm liq}}{\tau_{\rm fill}} \frac{\partial z}{\partial p_a}, \tag{10}$$

where $\partial p_a/\partial z$ is the ahydrostatic pressure gradient equal to the vertical component of the quantity in square brackets in Eq. (4). If the deformation term dominates over the negative buoyancy, then from Eq. (7), $\partial p_a/\partial z \sim h\rho g m$. The viscosity of liquid water is $\eta^{\rm liq} = 0.002$ Pa sec. For $m \sim 6 \times 10^{-5}\,\mathrm{m^{-1}}$, corresponding to a horizontal graben wavelength of 100 km, Eq. (10) implies that

$$k \sim 10^{-15}\left(\frac{10^6\ \text{years}}{\tau_{\rm fill}}\right)\mathrm{m^2}. \tag{11}$$

This is the permeability required to transport liquid water upward at the rate it is produced by tidal heating over a range of depths d. We can relate this permeability to melt fraction as follows. In real materials with dihedral angles less than 60°, at small melt fractions, the permeability typically depends on melt fraction as

$$k \sim k_0 a^2 f^2, \tag{12}$$

where a is grain size and $k_0 \sim 10^{-3}$ (Stevenson and Scott, 1991). Equating Eqs. (10) and (12), we can therefore solve for the average steady-state melt fraction if melt production within layer d is balanced by percolation of melt toward the surface:

$$f \sim \frac{1}{a}\left(\frac{h\eta^{\rm liq}}{k_0\tau_{\rm fill}}\frac{\partial z}{\partial p_a}\right)^{1/2}. \tag{13}$$

If we again take $\partial p_a/\partial z \sim h\rho g m$, then $f \sim 10^{-3}(1\,\mathrm{mm}/a) \times (10^6\ \text{years}/\tau_{\rm fill})$. Grain sizes are unknown but may be 0.1–1 mm (Kirk and Stevenson, 1987) which, for $\tau_{\rm fill} \sim 10^6$ years, implies that $f \sim 0.001–0.01$. For these melt fractions, the upward percolation rate of liquid water balances its production rate under plausible tidal heating. Physically, the idea is that the melt fraction self-adjusts to reach a steady state: if the melt fraction is too low, then percolation is inefficient and the melt fraction increases. If the melt fraction is too high, percolation is rapid and the melt fraction decreases. The strong dependence of permeability on melt fraction acts as a negative feedback that stabilizes the mean melt fraction to a value of 0.001–0.01.

Because the minimum depth of the partially molten regions on Ganymede is 5–10 km, and the uppermost lithosphere is extremely cold, the microscopic melt migration we have described must eventually give way to macroscopic flow along fractures within the uppermost 5–10 km of Ganymede's lithosphere. This situation is analogous to that for volcanism on Earth: melt is produced in rock at temperatures exceeding 1000 K, percolates upward, and eventually enters lenses or fractures, which enables it to reach the cold upper lithosphere without freezing en route. Exactly how the transition from microscopic to macroscopic transport occurs is poorly understood. Stevenson (1989) pointed out that a partially molten region undergoing shear deformation is subject to an instability that causes melt concentration, because regions of high melt fraction have low pressure and vice versa, which drives melt migration from regions of low melt fraction to regions of high melt fraction. On Earth, this process could produce magma lenses that eventually feed into fractures, and a similar process may be relevant on Ganymede.

Consider the conditions needed for liquid to reach the surface without freezing. Suppose that a vertical fracture extends from the surface to a source region of liquid water at 5–10 km depth and that liquid erupts onto the surface for a time $\tau_{\rm erupt}$. Over this time, heat will laterally diffuse a distance $(\kappa\tau_{\rm erupt})^{1/2}$ from the fracture, where $\kappa \approx 10^{-6}\,\mathrm{m^2\,sec^{-1}}$ is the thermal diffusivity. The average heat flux conducted laterally out of the fracture walls is $F \sim \rho c_p \Delta T (\kappa/\tau_{\rm erupt})^{1/2}$, where $c_p \approx 2000\,\mathrm{J\,kg^{-1}\,K^{-1}}$ is the specific heat of ice and $\Delta T \approx 120$ K is the temperature difference between the warm fracture and the surrounding cold ice. (This estimate includes only lateral heat conduction and neglects vertical heat loss from the fracture to the surface. This assumption is valid as long as $(\kappa\tau_{\rm erupt})^{1/2}$ is less than a few km and $\tau_{\rm erupt}$ is less than $\sim 3 \times 10^5$ years.) The heat lost from the fracture will cause the liquid water in the fracture to freeze. Over the course of the eruption, the volume of water that freezes, per unit length of the fracture along the surface, is $c_p \Delta T d (\kappa\tau_{\rm erupt})^{1/2}/L$, where L is the latent heat of melting and d is the vertical length of the fracture. If we want a substantial fraction of the liquid water to reach the surface without freezing, then the total eruption volume per unit length of the fracture along the surface, $\dot{v}\tau_{\rm erupt}$, must exceed the volume of water that freezes. This implies

$$\dot{v} \geqslant \frac{c_p \Delta T d}{L}\left(\frac{\kappa}{\tau_{\rm erupt}}\right)^{1/2} \approx 0.7\left(\frac{\text{years}}{\tau_{\rm erupt}}\right)^{1/2}\mathrm{m^2\,sec^{-1}}, \tag{14}$$

where $\dot{v}$ ($\mathrm{m^2\,sec^{-1}}$) is the volumetric eruption rate per length of fracture along the surface and $d = 5$ km has been used for the numerical estimate. ($\dot{v}$ can be viewed as the product of the fracture width and the vertical speed of liquid water ascending through the fracture.) Longer-duration eruptions require smaller effusion rates to prevent freezing because the

heat flux away from the fracture decreases with time. Eruptions lasting 1 and 100 years require effusion rates exceeding 0.7 and 0.07 $m^2\ sec^{-1}$, respectively. For a fracture 1 m wide, these rates correspond to vertical eruption velocities of 0.7 and 0.07 $m\ sec^{-1}$.

Notice that the fracture width does not enter Eq. (14) directly; liquid can reach the surface equally well in eruptions with rapid flow through narrow fractures or eruptions with slow flow through wide fractures, as long as $\dot{v}$ is sufficiently large (all that is required is that the total mass of liquid per time that flows through the fracture exceed the mass per time of liquid that freezes; the mass per time that freezes depends on eruption duration but not on fracture width). However, the fracture width plays an indirect role because wider fractures may allow larger effusion rates $\dot{v}$.

The above constraint on individual fractures can be combined with the global need to resurface bright terrain with a thickness $h \sim 1$ km of cryovolcanic flows. Suppose D is the average spacing between fractures that erupt, not necessarily simultaneously, within bright terrain. Then we must have $\dot{v}\tau_{\text{erupt}}/D \sim h$. Given a mean fracture spacing, we can use this constraint to eliminate τ_{erupt} from Eq. (14):

$$\dot{v} \geqslant \left(\frac{c_p \Delta T d}{L}\right)^2 \frac{\kappa}{hD} \approx 2 \times 10^{-6} \left(\frac{10\ \text{km}}{D}\right) \text{m}^2\ \text{sec}^{-1}, \tag{15}$$

where the numerical estimate uses $d = 5$ km and $h = 1$ km. For a given fracture spacing, this equation gives the minimum effusion rates that delivers 1 km of liquid to the surface without freezing en route. For 10-km fracture spacing, the corresponding eruption times are $\leqslant 2 \times 10^5$ years.

We expect that, once negatively buoyant liquid fills macroscopic fractures, the topographically induced pressure gradients can drive this liquid onto the surface in topographic lows. Envision a fluid-filled fracture extending from the partially molten region, at $\sim$ 5–10 km depth, to the free surface. Equation (7) implies that, at the center of a topographic low (i.e., $x = 0$), the difference in ahydrostatic pressure between depth d and depth zero, caused by the topography, is $\rho g h_0(1 - e^{-md})$. In comparison, the additional pressure at the base of the fluid-filled fracture, caused by the additional weight per area of the liquid, is $\Delta\rho g d$. Therefore, the pressure within the ice at the base of the fracture will exceed that of the liquid water in the fracture if $\rho g|h_0|(1 - e^{-md}) > \Delta\rho g d$. Such a pressure difference will cause the ice to deform, compacting the fracture and driving liquid water onto the surface. For long wavelengths, this condition can be approximately written as $|h_0|m > \Delta\rho/\rho$. For 100 km-wavelengths and $\Delta\rho/\rho = 0.08$, ascent of the liquid water in fluid-filled fractures occurs when $|h_0| \geqslant 1.3$ km.

Can fluid realistically be delivered to the surface at rates exceeding the lower limit of Eq. (15)? Many unresolved issues exist regarding melt segregation on Earth, but analytical and numerical calculations demonstrate that melt segregation into lenses and channels is a plausible end result of melt migration (e.g., Stevenson, 1989; Wiggins and Spiegelman, 1995). Consider a cylindrically shaped fluid-filled "magma chamber" of diameter d_c underlying a fluid-filled fracture extending to the surface within a graben. If the topographic pressure gradients overwhelm the negative buoyancy of fluid inside the fracture, and the magma chamber lies depth d below the surface, then there will be a pressure excess $\sim h\rho g m d$ between the ice and the fluid inside the magma chamber (here h is the graben depth). This pressure difference will drive compaction of the magma chamber and force fluid onto the surface. The strain rate in the ice resulting from this pressure difference is $h\rho g m d/\eta$, where η is the viscosity of the ice surrounding the magma chamber. This strain rate can be equated to the fractional rate of change of magma chamber volume, $\dot{v}/d_c^2$. This implies that

$$\dot{v} \sim \frac{h\rho g m d d_c^2}{\eta}. \tag{16}$$

For $d \sim 10$ km, $h \sim 1$ km, $m \sim 6 \times 10^{-5}\ \text{m}^{-1}$, $d_c \sim 1$ km, and $\eta \sim 10^{14}$ Pa sec, $\dot{v} \sim 0.01\ \text{m}^2\ \text{sec}^{-1}$. This effusion rate exceeds the lower limit by four orders of magnitude and suggests that, if melt can segregate into $\sim$ 1-km-wide lenses, then the melt can be easily delivered onto the surface—in topographic lows—before freezing.

The fact that warm, soft ice underlies the surface implies that the graben will be gravitationally relaxing while the resurfacing occurs. To produce bright terrain, the graben must fill before they gravitationally relax, implying that $\tau_{\text{relax}} > \tau_{\text{fill}}$. Therefore, for liquid–water cryovolcanic production of bright terrain to occur, the gravitational relaxation timescale must exceed 10^6 years. Gravitational relaxation has a contentious history for icy satellites. Early, purely viscous calculations of the relaxation process implied that the relaxation time for craters is short ($< 10^8$ years) even for a cold, isothermal interior (an assumption that maximizes the relaxation time), implying that Ganymede and Callisto's craters should have all completely relaxed, contrary to observations (Thomas and Schubert, 1988). Studies attempting to quantify the effects of elasticity on the relaxation have obtained contradictory results (Hillgren and Melosh, 1989; Dombard, 2000). To date, the most thorough analysis has been performed by Dombard and McKinnon (2000) and Dombard (2000); they included the latest ice rheological data (Goldsby and Kohlstedt, 2001) and plastic effects as well as elasticity. Dombard and McKinnon (2000) showed that a cold, isothermal icy satellite can indeed maintain topography over 10^{10} year timescales, helping to resolve the puzzle raised by Thomas and Schubert (1988). However, Ganymede thermal models predict that the heat flux in absence of tidal heating should be perhaps a few mW m^{-2} (Kirk and Stevenson, 1987; Mueller and McKinnon, 1988). When steep temperature gradients are included extending downward from a surface temperature of 120 K, the relaxation times are 10^3–10^8 years depending on the exact thermal profile and landform diameter (Dombard, 2000). Taken at face value, such short relaxation times are problematic

for our cryovolcanism model, as well as for a general understanding of crater retention under plausible heat flows on the icy satellites. However, several mechanisms exist for lengthening the relaxation times, which may help resolve the discrepancy. First, Dombard assumed a grain size of 1 mm, but, as he pointed out, order-of-magnitude increases in the grain size can cause order-of-magnitude increases in the viscosity and hence relaxation time. Second, low surface temperatures, as may exist at high latitudes if the regolith is not strongly insulating, promote longer relaxation times. Third, Dombard's calculations assumed flow within a deep, constant-density layer; if the ice shell was thin at the time of resurfacing, or if Ganymede has a low-density crust, the near-surface flow would be confined to a channel that would increase the relaxation time substantially (e.g., Nimmo and Stevenson, 2001). Fourth, if the high thermal gradients occurred only episodically or were spatially confined to narrow regions underneath the graben (e.g., the result of runaway heating along fractures; Nimmo and Gaidos, 2002), then the average thermal gradient affecting relaxation would be smaller, promoting longer relaxation times. Fifth, dynamically induced topography associated with lateral density contrasts can be retained much longer than topography in a constant-density medium; for example, Earth's mantle convection can produce dynamic topography with lifetimes of 10^8 years or more despite the fact that the postglacial-rebound timescale (which is effectively what Dombard calculated) is 10^4 years. On Ganymede, lateral density contrasts might be associated with lateral differences in salinity (possibly coupled to thermal convection in the ice layer) or silicate loading of the ice layer (perhaps resulting from an uneven spatial distribution of impact-crater ejecta). Detailed numerical studies of the relaxation process will be needed to quantify these effects.

2.2. Topographic resurfacing by slush

Although liquid–water resurfacing is attractive, we have pointed out two difficulties: (i) the large negative buoyancy of pure liquid water relative to pure ice ensures that liquid can only be pumped to the surface from 5–10 km depth, which in turn requires large tidal heating rates to produce liquid at such shallow depths, and (ii) the gravitational relaxation times are potentially shorter than the inferred minimum time to melt, transport to the surface, and refreeze a ~ 1 km-deep layer of liquid water. Resurfacing by slush—a matrix of ice with a few percent or less liquid water—provides an alternative that helps ameliorate these problems. If crustal extension can produce open extension fractures > 100 m wide on graben floors, then the topographic pressure gradients associated with the graben may be able to drive macroscopic bodies of slush through these conduits onto the graben floors.

Slush can be close to neutrally buoyant, so the net pressure gradients the slush experiences are close to those in Figs. 4b and 5b. Underneath topographic lows, therefore, the slush can experience a net upward pressure-gradient force at depths greater than 20 km, depending on the wavelength of the topography. Slush can thus be driven upward from depths > 20 km, far exceeding the depth from which liquid water can easily be pumped. Futhermore, because the slush is almost neutrally buoyant, the depth from which the slush can be pumped is almost independent of the topographic amplitude (unlike the liquid–water case, where large-amplitude topography was needed to counteract the large negative buoyancy of the liquid). Therefore, graben with a relatively modest depth (e.g., ~ 1 km) can suffice for driving slush upward.

The gravitational relaxation problem is less severe for slush resurfacing than liquid–water resurfacing. The fact that the topographic pressure gradients can drive slush upward from greater depth than liquid water implies that, at least initially, the vertical thermal gradient dT/dz can be lower for slush resurfacing than for liquid–water resurfacing (since melting temperature is reached at ~ 20 km in the former case but at 5–10 km-depth in the latter case). This allows greater gravitational relaxation time scales. Furthermore, since only a few percent of the mass of slush is liquid, a given volume of slush can be produced more easily than the same volume of liquid. Under plausible tidal heating rates, the minimum timescale needed to produce enough slush to fill the graben, $\tau_{\rm fill}$, may then be $\sim 10^4$–10^5 years rather than 10^6 years as for the liquid case.

The key problem with slush is how to transport it through the uppermost cold lithosphere to the surface. Partially molten rocks and ice with melt fractions of a few percent have viscosities typically ten times lower than that of solid rock or ice at the melting temperature (Kohlstedt and Zimmerman, 1996; De La Chapelle et al., 1999). Therefore the slush viscosity is still large, $\sim 10^{12}$–10^{13} Pa sec, and thus the conduits through which slush reaches the surface must be wide. The pressure gradient driving the slush is approximately ρghm (Eq. (7)), which implies a driving force per fracture-wall area $\rho ghml$, where l is the width of the fracture through which slush ascends to the surface. This force per area is resisted by the viscous shear stress $\sim \eta w/l$, where w is the vertical ascent velocity of the slush through the fracture. Balancing these forces and equating the ascent time to d/w, where d is the vertical length of the fracture, gives an ascent time of $\eta d/(\rho ghml^2)$. For slush to reach the surface, the ascent time must be less than the thermal diffusion time, l^2/κ; otherwise, the slush will cool, stiffen, and stall. Thus slush can reach the surface only if

$$l \geqslant \left(\frac{\eta d\kappa}{\rho ghm}\right)^{1/4}, \tag{17}$$

which is $\sim 10^2$ m for slush viscosities of 10^{12}–10^{13} Pa sec. It remains unclear whether open conduits $> 10^2$ m wide would actually form; the extension might instead be accomodated by slip along normal faults, effectively precluding the upward transport of slush. Additional issues also remain; for example, the volcanism might produce km-tall lobate scarps,

which are not observed; furthermore, it is not obvious how large masses of slush will transition from diapiric-type flow in the deep subsurface to flow along fractures within the lithosphere. But the mechanism warrants further study, and we emphasize that despite the above challenges the same advantages exist as for topographic pumping of liquid water—eruptions are confined to topographic lows and cease once the graben fill. Detailed numerical simulations are required to evaluate the mechanism further, and we leave these for the future.

3. Alternate resurfacing mechanisms

3.1. Buoyant migration of liquid water to the surface

If the lithosphere above the minimum depth of melting has an average density greater than that of liquid water, the liquid can migrate to the surface, helping to produce bright terrain. Such a dense upper lithosphere may be caused by silicate contamination from asteroidal or cometary impact. Galileo gravity data imply that Ganymede is strongly differentiated at present (Anderson et al., 1996), and thermal models (Schubert et al., 1981; McKinnon and Parmentier, 1986) suggest at least partial differentiation during accretion. This process would flush the surface layers of rock, leaving a relatively pure ice lithosphere. Subsequent impacts would contaminate the upper lithosphere with silicates (e.g., Prockter et al., 1998). Our goal is to calculate the lithospheric silicate mass loading by considering the impact histories displayed in the cratering record.

We start with crater statistics from Strom et al. (1981), who presented crater counts as a function of crater diameter for diameters exceeding 4 km on Ganymede and 11 km on Callisto. As yet, no updates to these global size distributions have been published, although size distributions for small craters (Prockter et al., 1998; Ivanov and Basilevsky, 2002) and photogeological studies of individual craters (Greeley et al., 2001; Schenk and Ridolfi, 2002) have recently been published using Galileo data. Interestingly, the Strom et al. (1981) crater densities on Callisto exceed those in Ganymede's dark terrain by a factor of 2–3, suggesting that even Ganymede's most ancient surfaces are not primordial. Callisto may therefore preserve the more relevant record of total bombardment in the jovian system. To account for the fact that Jupiter's gravitational focusing should lead to more impacts on Ganymede than Callisto, we double Callisto's crater density for use with Ganymede.

For each crater size, we calculate the transient crater diameter from the observed diameter using the relation from McKinnon and Schenk (1995):

$$D_{\mathrm{tr}} = 0.864\left(\frac{D_{\mathrm{f}}}{\mathrm{km}}\right)^{0.9025}\ \mathrm{km}, \tag{18}$$

where D_{tr} and D_{f} are the transient and final diameters. The transient crater volume V is calculated from the transient diameter assuming the transient crater is a paraboloid of revolution with a diameter $2\sqrt{2}$ times its depth, which implies that $V = \pi D_{\mathrm{tr}}^3/(16\sqrt{2})$. We then compute the impactor mass m using Schmidt–Holsapple gravity scaling. Although both strength and gravity effects are important for craters smaller than 20-km diameter, the majority of the mass is contained in the largest impactors, where gravity scaling suffices. The impactor mass is then given by

$$m = \rho\left(\frac{V}{K}\right)^{3/(3-\alpha)}\left[\frac{g}{u^2}\left(\frac{3}{4\pi}\right)\right]^{3\alpha/(3-\alpha)}, \tag{19}$$

where V is the transient crater volume, ρ is target density, u is impact speed, g is surface gravity, and K and α are dimensionless parameters that depend on the material properties of the target. We use an impactor speed of 15 km s^{-1}, the escape velocity of Jupiter at the distance of Ganymede. The adopted material parameters, $K = 0.2$ and $\alpha = 0.65$, are appropriate to a soft rock target (see Holsapple, 1993) and are probably relevant for ice, although we also test values of K varying by a factor of ~ 2 and α varying by $\sim 30\%$, since the uncertainties are of this order. We then sum the impactor masses over all observed craters. By assuming that the ejecta is evenly mixed to a depth of several km and evenly spread around the globe, we can calculate the increase in density of the uppermost lithosphere.

The calculations show that for crater diameters ~ 5–10^3 km, mass flux is dominated by the largest impacts. In all cases, craters less than 256 km in diameter (taken together) produce a density increase only a few percent of that needed to allow liquid to reach the surface from several km depth. In all cases, the largest impactors also provide insufficient material to allow liquid to reach the surface (by a factor ~ 10 for nominal K and α). Using $K = 0.1$ and $\alpha = 0.5$ allows larger impactors for a given crater size, but still provides insufficient silicate loading. If much of the impactor mass escapes back to space during the impacts, as suggested by hydrodynamic modeling (Pierazzo and Chyba, 2002), then the gap between the actual contamination and that needed to allow buoyant ascent of liquid is exacerbated still further. However, we assumed the material is globally distributed, which is unlikely: material is probably dropped into an ejecta blanket near the crater, rather than globally. Furthermore, although Callisto is geometrically unsaturated (its density of > 30 km-diameter craters is much less than that in the lunar highlands), an equilibrium could exist wherein formation of new craters causes obliteration of older craters, in which case the adopted crater density provides only a lower limit on the mass that has impacted the surface. Possibly, then, some local ejecta blankets or other regions could have sufficient silicate loading to allow buoyant migration of water to the surface from a few km depth.

However, bright–dark terrain boundaries are generally smooth and curvilinear over $\sim 10^2$–10^3 km distances. This observation strongly suggests that resurfacing was confined to a global system of graben. Lithospheric regions covered by thick, dense ejecta blankets would tend to become

graben rather than horst, facilitating resurfacing on graben floors. However, very few regions where resurfacing embayed craters and other topography have been found, and it is doubtful that resurfacing by this mechanism would have occurred *only* at the graben floors, and would never have spilled over the top of graben.

3.2. Pumping of water to surface by compressive stress

When tidal heating occurs, spatial variations in the heating rate may cause spatial temperature variations, and the differential thermal expansion associated with these temperature variations can produce stresses available for pumping liquid water to the surface. In the most extreme case, a thermal runaway occurs in a confined region that is fully encased in cold, elastic ice. The thermal expansion that occurs during warming will produce a compressive stress, which may allow cracks to penetrate to the surface and liquid water to be pumped to the surface. To order of magnitude, the pressure increase within the region undergoing runaway is

$$\Delta p \sim K \alpha \Delta T, \tag{20}$$

where K is the bulk modulus, α is thermal expansivity, and ΔT is the temperature increase occurring during the runaway. For probable values ($K \sim 10^{10}$ Pa, $\alpha \sim 10^{-4}$ K^{-1}, and $\Delta T \sim 50$ K), this implies $\Delta p \sim 500$ bars. In practical terms, the cold ice surrounding the runaway will fracture once the overpressurization reaches the 10–100-bar yield strength of the ice, so the maximum overpressurization is actually 10–100 bars (or even less if the ice is already fractured). The maximum amount of water that can be pumped to the surface is that which, because of the compaction associated with mass loss, reduces the pressure increase Δp to zero. If water pools on the surface in a linear region of width L and depth h, and if the runaway occurs within a linear region a region of width and vertical extent l, then the depth of liquid water that reaches the surface is roughly

$$h \sim \frac{l^2 \Delta p}{K L}. \tag{21}$$

If we assume the water pools only over the runaway (i.e., $l \sim L$), let $l \sim 10$ km, and use $\Delta p \sim 10$–100 bars, then $h \sim$ 1–10 m. If instead we require the water to pool over a region 10^2 km wide (roughly the size of individual bright-terrain units), we get $h \sim 0.1$–1 m. These are upper limit, for two reasons. First, much of the liquid may be pushed down rather than up. Second, the runaway can only lead to overpressurization if it is fully encased within cold, elastic ice, but this condition is severe and may not be achieved on Ganymede. The cold ice must be elastic on the timescale of the runaway, which implies that the viscosity $\eta > K \tau_{\text{runaway}}$. For a runaway time scale of 10^6 years, this requires $\eta > 10^{23}$ Pa sec, implying extremely low temperatures in the background ice (perhaps < 150 K). This condition is unlikely to be satisfied at depths greater than a few km even for modest thermal gradients. The estimate in Eq. (21) is therefore an upper limit. These amounts of liquid are significantly less than the ~ 1 km inferred thickness of the resurfaced regions. Thus, although this process may have occurred on Ganymede, it is unlikely to explain bright terrain formation.

4. Conclusions

Although cryovolcanic flooding of low-lying graben has been a long-favored model for producing Ganymede's bright terrain (Parmentier et al., 1982), there have been no plausible mechanisms to explain how vast quantities of material were transported to the surface, why the eruptions were confined to graben floors, and why such floods did not overflow the graben. Here we presented models to overcome these problems. In a global and time-averaged sense, tidal heating within an ancient Laplace-like resonance can cause a heat flux between 10–100 mW m^{-2}, and even larger fluxes may occur episodically via geophysical feedbacks and time variability in the orbital history. Episodic melting at depths of 5–10 km is a plausible outcome of such a resonance. The tidal heating can produce a global subsurface ocean several hundred km thick, which allows the satellite to expand by $\sim 1\%$ and provides a plausible mechanism for producing graben (Showman et al., 1997). The topography associated with these graben generates subsurface pressure gradients that can drive upward Darcy flow of subsurface pore–space liquid water beneath topographic lows despite the negative buoyancy of the liquid. This provides a realistic way of resurfacing Ganymede with liquid water. Once on the surface, the tops of the liquid–water flows would freeze, providing an insulating crust and lengthening cooling times enough for the flows to fill the graben floors (Allison and Clifford, 1987). For plausible topographic amplitudes and ice–liquid density contrasts, the maximum depth from which liquid can be pumped to the surface is 10–20 km. Because the Darcy flow is only upward underneath topographic lows, the model can explain why eruptions were confined to graben floors (rather than occurring on adjacent high-standing dark terrain) and ceased once the graben were filled. The model therefore provides an attractive explanation for the generally straight bright–dark terrain boundaries and the absence of volcanic flow features across dark terrain. A possible problem is that at least 10^6 years is required to generate and transport to the surface sufficient liquid water to submerge craters and other landforms, but recent studies (Dombard, 2000) suggest that the graben may gravitationally relax before they can flood sufficiently. The relaxation time depends on several poorly known parameters, however, and mechanisms exist that will allow longer relaxation times; more detailed calculations are needed to resolve this issue for our model. Resurfacing by slush provides an alternative that helps overcome some of the difficulties associated with liquid–water volcanism, although it is unclear whether wide enough lithospheric conduits

existed for subsurface slush to actually get onto the surface.

We also considered alternate mechanisms for transporting liquid water to the surface from ~ 10-km depths, including pumping by differential thermal expansion stresses and buoyant rise of liquid water to the surface through a silicate-laden lithosphere that is denser than liquid water. Each of these mechanisms has problems, however, leading us to favor the "topographic pumping" mechanism.

The topography associated with craters also produces subsurface pressure gradients, and although some crater floors contain cryvolcanic flow-like features (Schenk and Moore, 1995), the general lack of bright-terrain patches on the floors of dark-terrain craters needs explaining. A natural explanation is that newly formed graben were weak zones, causing enhanced tidal flexing and heating and allowing shallow melting underneath graben but not underneath most craters. This would allow topographic pumping of liquid water onto graben floors while, underneath most craters, no liquid water existed at the appropriate depths (5–20 km) for upward pumping of liquid water to occur.

The bright terrain formed over an extended ~ 10^8 year period perhaps 1 to 3 byr ago (Shoemaker et al., 1982; Zahnle et al., 1998), and relatively little, if any, cryovolcanic activity seems to have occurred since that time. Because the Laplace resonance does not pump Ganymede's eccentricity, Ganymede would naturally become dormant after the Laplace resonance was established, so the termination of activity was probably a direct result of the orbital evolution. What controlled the length of the resurfacing episode is less clear, but it may reflect the duration of the Laplace-like resonance that pumped Ganymede's eccentricity or, if the resonance lasted longer than the resurfacing epoch, an episode where the tidal Q values of Jupiter, Io, and Ganymede conspired to produce unusually high eccentricities and tidal heating rates in Ganymede. For example, coupled geophysical-orbital feedbacks can produce 10^7–10^8 year-long spikes in the tidal-heating rate (Showman et al., 1997).

Acknowledgments

We thank D.J. Stevenson, W.B. McKinnon, F. Nimmo, P. Schenk, A. Dombard, and R. Strom for useful discussions. Bill Moore and an anonymous reviewer provided many helpful comments. This work was supported by NSF grant AST-0206269 and by a grant from the NASA PG&G program to A.P.S.

References

Allison, M.L., 1982. Constraints on the nature and evolution of Ganymede's crust. In: Proc. Lunar Planet. Sci. Conf. 13th, pp. 11–12.

Allison, M.L., Clifford, S.M., 1987. Ice-covered water volcanism on Ganymede. J. Geophys. Res. 92, 7865–7876.

Anderson, J.D., Lau, E.L., Sjogren, W.L., Schubert, G., Moore, W.B., 1996. Gravitational constraints on the internal structure of Ganymede. Nature 384, 541–543.

Collins, G.C., Head, J.W., Pappalardo, R.T., 1998. The role of extensional instability in creating Ganymede's grooved terrain: insights from Galileo high-resolution stereo imaging. Geophys. Res. Lett. 25, 233–236.

Collins, G.C., Head, J.W., Pappalardo, R.T., 2000. A global database of grooves and dark terrain on Ganymede, enabling quantitative assessment of terrain features. In: Proc. Lunar Planet. Sci. Conf. 31st. Abstract #1034 [CD-ROM].

Croft, S.K., Lunine, J.I., Kargel, J., 1988. Equation of state of ammonia–water liquid: derivation and planetological applications. Icarus 73, 279–293.

De La Chapelle, S., Milsch, H., Castelnau, O., Duval, P., 1999. Compressive creep of ice containing a liquid intergranular phase: rate-controlling processes in the dislocation creep regime. Geophys. Res. Lett. 26, 251–254.

Dombard, A.J., 2000. Modeling of geodynamic processes on Ganymede and Callisto: insight into thermal and tectonic histories. PhD dissertation. Univ. Washington, Saint Louis, Missouri.

Dombard, A.J., McKinnon, W.B., 2000. Long-term retention of impact crater topography on Ganymede. Geophys. Res. Lett. 27, 3663–3666.

Dombard, A.J., McKinnon, W.B., 2001. Formation of grooved terrain on Ganymede: extensional instability mediated by cold, superplastic creep. Icarus 154, 321–336.

Golden, K.M., Ackley, S.F., Lytle, V.I., 1998. The percolation phase transition in sea ice. Science 282, 2238–2241.

Goldreich, P., Soter, S., 1966. Q in the Solar System. Icarus 5, 375–389.

Goldsby, D.L., Kohlstedt, D.L., 2001. Superplastic deformation of ice: experimental observations. J. Geophys. Res. 106, 11017–11030.

Golombek, M.P., Allison, M.L., 1981. Sequential development of grooved terrain and polygons on Ganymede. Geophys. Res. Lett. 8, 1139–1142.

Greeley, R., Heiner, S., Klemaszewski, J.E., 2001. Geology of Lofn crater, Callisto. J. Geophys. Res. 106, 3261–3273.

Head, J.W., Pappalardo, R., Collins, G., Greeley, R., 1997. Tectonic resurfacing on Ganymede and its role in the formation of grooved terrain. In: Proc. Lunar Planet. Sci. Conf. 28th, pp. 535–536. Abstract.

Head, J.W., Pappalardo, R., Kay, J., Collins, G., Prockter, L., Greeley, R., Chapman, C., Carr, M., Belton, M.J.S., the Galileo imaging team, 1998. Cryovolcanism on Ganymede: evidence in bright terrain from Galileo solid state imaging data. In: Proc. Lunar Planet. Sci. Conf. 29th. Abstract #1666.

Head, J., 10 colleagues, 2002. Evidence for Europa-like tectonic resurfacing styles on Ganymede. Geophys. Res. Lett. 29 (24), 2151.

Hillgren, V.J., Melosh, H.J., 1989. Crater relaxation on Ganymede: implications for ice rheology. Geophys. Res. Lett. 16, 1339–1342.

Holsapple, K.A., 1993. The scaling of impact processes in planetary sciences. Annu. Rev. Earth Planet. Sci. 21, 333–373.

Hogenboom, D.L., Kargel, J.S., Ganasan, J.P., Lee, L., 1995. Magnesium sulfate–water to 400 MPa using a novel piezometer: densities, phase equilibria, and planetological implications. Icarus 115, 258–277.

Hogenboom, D.L., Kargel, J.S., Consolmagno, G.J., Holden, T.C., Lee, L., Buyyounouski, M., 1997. The ammonia–water system and the chemical differentiation of icy satellites. Icarus 128, 171–180.

Houben, H., Young, R.E., Showman, A., Mosqueira, I., 2001. Full hydrodynamic calculations of tidal dissipation in Jupiter. In: Jupiter: Planet, Satellites, and Magnetosphere. Conf. June 25–30, 2001, Boulder, CO. Abstract, p. 51.

Ioannou, P.J., Lindzen, R.S., 1993. Gravitational tides in the outer planets. II. Interior calculations and estimation of the tidal dissipation factor. Astrophys. J. 406, 266–278.

Ivanov, M.A., Basilevsky, A.T., 2002. Morphology and size-frequency distribution of kilometer-scale impact craters on Callisto and Ganymede derived from Galileo data. Solar System Res. 36, 447–457.

Kargel, J.S., 1991. Brine volcanism and the interior structures of asteroids and icy satellites. Icarus 94, 368–390.

Ketcham, W.M., Hobbs, P.V., 1969. An experimental determination of surface energies of ice. Philos. Mag. 19, 1161–1173.
Kirk, R.L., Stevenson, D.J., 1987. Thermal evolution of a differentiated Ganymede and implications for surface features. Icarus 69, 91–134.
Kohlstedt, D.L., Zimmerman, M.E., 1996. Rheology of partially molten mantle rocks. Annu. Rev. Earth Planet. Sci. 24, 41–62.
Mader, H.M., 1992. Observations of the water-vein system in polycrystalline ice. J. Glaciol. 38, 333–347.
Malhotra, R., 1991. Tidal origin of the Laplace resonance and the resurfacing of Ganymede. Icarus 94, 399–412.
McKenzie, D., 1984. The generation and compaction of partially molten rock. J. Petrology 25, 713–765.
McKinnon, W.B., Parmentier, E.M., 1986. Ganymede and Callisto. In: Satellites. Univ. of Arizona Press, Tucson, pp. 718–763.
McKinnon, W.B., Schenk, P.M., 1995. Estimates of comet fragment masses from impact crater chains on Callisto and Ganymede. Geophys. Res. Lett. 22, 1829–1832.
Mueller, S., McKinnon, W.B., 1988. Three-layered models of Ganymede and Callisto: compositions, structures, and aspects of evolution. Icarus 76, 437–464.
Murchie, S.L., Head, J.W., Helfenstein, P., Plescia, J.B., 1986. Terrain types and local-scale stratigraphy of grooved terrain on Ganymede. In: Proc. Lunar Planet. Sci. Conf. 17th, Part 1. J. Geophys. Res. 91, E222–E238.
Nimmo, F., Gaidos, E.J., 2002. Thermal consequences of strike-slip motion on Europa. J. Geophys. Res. 107 (E11), 5021.
Nimmo, F., Stevenson, D.J., 2001. Estimates of martian crustal thickness from viscous relaxation of topography. J. Geophys. Res. 106, 5085–5098.
Nimmo, F., Pappalardo, R.T., Giese, B., 2002. Effective elastic thickness and heat flux estimates on Ganymede. Geophys. Res. Lett. 29. 62-1–62-4.
Pappalardo, R.T., Collins, G.C., 1999. Extensionally strained craters on Ganymede. In: Proc. Lunar Planet. Sci. Conf. 30th. Abstract #1773.
Pappalardo, R.T., 15 colleagues, 1998. Grooved terrain on Ganymede: first results from Galileo high-resolution imaging. Icarus 135, 276–302.
Pappalardo, R.T., Collins, G.C., Head, J.W., Helfenstein, P., McCord, T.B., Moore, J.M., Prockter, L.M., Schenk, P.M., Spencer, J.R., 2004. Geology of Ganymede. In: Jupiter: Planet, Satellites, and Magnetosphere. Cambridge Univ. Press, Cambridge.
Parmentier, E.M., Squyres, S.W., Head, J.W., Allison, M.L., 1982. The tectonics of Ganymede. Nature 295, 290–293.
Patel, J.G., Pappalardo, R.T., Head, J.W., Collins, G.C., Hiesinger, H., Sun, J., 1999. Topographic wavelengths of Ganymede groove lanes from Fourier analysis of Galileo images. J. Geophys. Res. 104, 24057–24074.
Pierazzo, E., Chyba, C.F., 2002. Cometary delivery of biogenic elements to Europa. Icarus 157, 120–127.
Prockter, L.M., 2001. Icing Ganymede. Nature 410, 25–26.
Prockter, L.M., 14 colleagues, 1998. Dark terrain on Ganymede: geological mapping and interpretation of Galileo Regio at high resolution. Icarus 135, 317–344.
Schenk, P.M., Moore, J.M., 1995. Volcanic constructs on Ganymede and Enceladus: topographic evidence from stereo images and photoclinometry. J. Geophys. Res. 100, 19009–19022.
Schenk, P.M., Ridolfi, F.J., 2002. Morphology and scaling of ejecta deposits on icy satellites. Geophys. Res. Lett. 29 (12).
Schenk, P.M., McKinnon, W.B., Gwynn, D., Moore, J.M., 2001. Flooding of Ganymede's bright terrains by low-viscosity water-ice lavas. Nature 410, 57–60.
Schubert, G., Stevenson, D.J., Ellsworth, K., 1981. Internal structures of the galilean satellites. Icarus 47, 46–59.
Scott, D.R., 1988. The competition between percolation and circulation in a deformable porous medium. J. Geophys. Res. 93, 6451–6462.
Shoemaker, E.M., Lucchitta, B.K., Wilhelms, D.E., Plescia, J.B., Squyres, S.W., 1982. The geology of Ganymede. In: Satellites of Jupiter. Univ. of Arizona Press, Tucson, pp. 435–520.
Showman, A.P., Malhotra, R., 1997. Tidal evolution into the Laplace resonance and the resurfacing of Ganymede. Icarus 127, 93–111.
Showman, A.P., Malhotra, R., 1999. The galilean satellites. Science 286, 77–84.
Showman, A.P., Stevenson, D.J., Malhotra, R., 1997. Coupled orbital and thermal evolution of Ganymede. Icarus 129, 367–383.
Spiegelman, M., McKenzie, D., 1987. Simple 2-D models for melt extraction at mid-ocean ridges and island arcs. Earth Planet. Sci. Lett. 83, 137–152.
Squyres, S.W., 1981. The topography of Ganymede's grooved terrain. Icarus 46, 156–168.
Stevenson, D.J., 1983. Anomalous bulk viscosity of two-phase fluids and implications for planetary interiors. J. Geophys. Res. 88, 2445–2455.
Stevenson, D.J., 1989. Spontaneous small-scale melt segragation in partial melts undergoing deformation. Geophys. Res. Lett. 16, 1067–1070.
Stevenson, D.J., Scott, D.R., 1991. Mechanics of fluid-rock systems. Annu. Rev. Fluid. Mech. 23, 305–339.
Strom, R.G., Woronow, A., Gurnis, M., 1981. Crater populations on Ganymede and Callisto. J. Geophys. Res. 86, 8659–8674.
Thomas, P.J., Schubert, G., 1988. Power-law rheology of ice and the relaxation style and retention of craters on Ganymede. J. Geophys. Res. 93, 13755–13762.
Turcotte, D.L., Schubert, G., 2002. Geodynamics, second ed. Cambridge Univ. Press, New York.
Walford, M.E.R., Nye, J.F., 1991. Measuring the dihedral angle of water at a grain boundary in ice by an optical diffraction method. J. Glaciol. 37, 107–112.
Walford, M.E.R., Roberts, D.W., Hill, I., 1987. Optical measurements of water lenses in ice. J. Glaciol. 33, 159–161.
Wiggins, C., Spiegelman, M., 1995. Magma migration and magmatic solitary waves in 3-D. Geophys. Res. Lett. 22, 1289–1292.
Zahnle, K., Dones, L., Levison, H.F., 1998. Cratering rates on the galilean satellites. Icarus 136, 202–222.